SI: Interplay of acoustophoresis and dielectrophoresis in a standing surface acoustic wave field: from spherical to non-spherical particles

Sebastian Sachs, David Schreier, Christian Cierpka, and Jörg König
Institute of Thermodynamics and Fluid Mechanics,
Technische Universität Ilmenau, P.O. Box 100565, 98684 Ilmenau, Germany

Felix Brand and Klaus Stefan Drese
Coburg University of Applied Sciences and Arts, ISAT - Institute of Sensor and Actuator Technology, 96450 Coburg, Germany

I. INFLUENCE OF THE METAL LAYER ON THE SAW AMPLITUDE

In Fig. S1, the normalized amplitude of the SAW $\tilde{A}$ in the regions of free and metallized substrate surface is depicted as a result of measurements using LDV (see section 2.3). The experimentally derived amplitude was averaged between three lines parallel to the aperture of the IDTs. The profile features typical local maxima symmetrical to the center of the aperture ($y/AP = 0$) due to diffraction of the SAW. The inhomogeneous amplitude of the SAW in y-direction translates into the sSAW used to manipulate suspended particles. Due to the gradients in the displacement field, three-dimensional acoustically induced vortex structures (see Fig. S6, SI, [1, 2]) as well as local peaks in the acoustic pressure and electric field arise in the outer regions of the sSAW. While this study focuses on the phenomena in the center of the sSAW, the influence of the local maxima in the sSAW amplitude on the behavior of spherical and non-spherical particles is highly relevant for further investigations. In the region of the metallized substrate surface, additional periodic diffraction patterns occur with lower amplitude. However, the metal layer has only a marginal influence on the amplitude of the SAW, leading to similar acoustic fields in both regions of the micro channel.

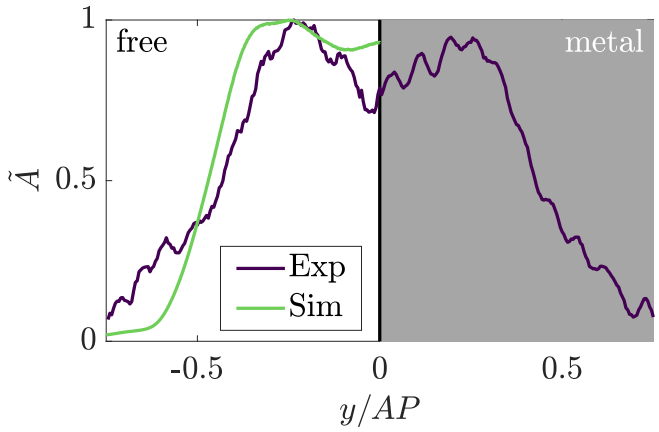

FIG. S1. Experimentally (Exp) and numerically (Sim) derived normalized amplitude of the surface displacement $\tilde{A}$ normal to the substrate surface. The profile along the main flow direction (y) extend across the free and metallized substrate surface.

The measured amplitude of the normal displacement component allows comparison with the numerically calculated SAW amplitude in the region of the free substrate surface. In the simulation, only a travelling SAW was considered, which is completely damped by perfectly matched layers (PML) at the edge of the substrate (see section **??**). The numerical model includes the $LiNbO_3$ substrate, an IDT with 20 electrode pairs and neither the metal layer nor the micro channel. A local maximum occurs in the profile of the numerically calculated amplitude analogous to the measured profile. Differences between the measured and calculated amplitude might be caused by the lower number of electrode pairs in the numerical model, which was limited due to the numerical effort. However, the significant features of the amplitude profile are resolved numerically, resulting in a good agreement between simulation and experiment.

II. NUMERICAL SIMULATION

A. Boundary conditions and material properties

The propagation of the surface acoustic waves (SAWs) and the associated electrical potential as well as the radiation of mechanical and electrical energy in the fluid domain were numerically calculated in a full three-dimensional model. The model includes the piezoelectric substrate of lithium niobate (LN), the fluid domain and polydimethylsiloxane (PDMS)

domain (see Fig. S2). The computational domains are surrounded by perfectly matched layers (PMLs, [3]) to model the full attenuation of the acoustic and electric fields in infinite space. By inserting a symmetry boundary condition in the yz-plane at $x = 0\,\mu\text{m}$, only half of the acoustoelectronic device is modeled, which drastically reduces the numerical effort. All domains extend over 3.2 mm in y-direction. The fluid domain covers a cross-section of $250 \times 180\,\mu\text{m}^2$ and is enveloped by PDMS with an extension of 1000 µm in x-direction and 380 µm in z-direction. The lithium niobate substrate is 500 µm thick and extends 3.8 mm in x-direction. 20 pairs of electrodes are defined as areas of $AP \times \lambda_{\text{SAW}}/4$ with alternating potential $\phi_0 = \pm 10\,\text{V}$ on the substrate surface. Here, the aperture of the interdigital transducers (IDTs) and the wavelength of the SAW are denoted by AP and λ_{SAW}, respectively. A zero charge boundary condition is applied on the remaining substrate surface, i.e. $\boldsymbol{n} \cdot \boldsymbol{D} = 0$.

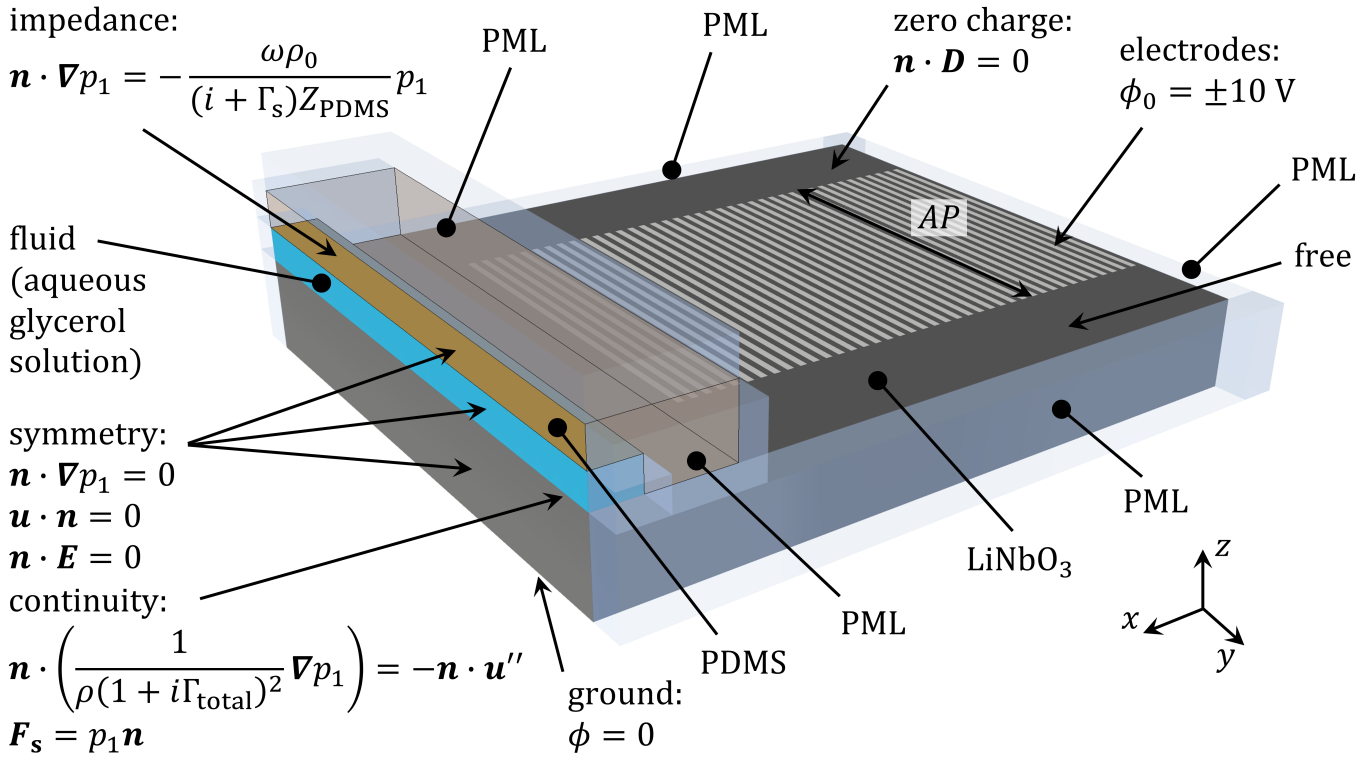

FIG. S2. Schematic of the full numerical model with fluid, PDMS and piezoelectric lithium niobate domain surrounded by PMLs. The associated boundary conditions of the coupled calculation using the "Pressure Acoustic", "Solid Mechanics" and "Electrostatics" interfaces in Comsol Multiphysics are indicated.

The alternating potential at the electrodes leads to periodic surface deformations, which propagate as SAWs along the substrate surface. Using the "Piezoelectric Effect" multiphysics coupling, the calculation is performed by coupling the "Solid Mechanics" and "Electrostatics" interface in Comsol Multiphysics (version 6.1, [4]). The bottom of the LN substrate is electrically grounded, i.e. $\phi = 0$. The elastic surface deformation is coupled via an "Acoustic-Structure Boundary" into the fluid domain, in which the acoustic fields are numerically solved using the "Pressure Acoustics" interface. For this, the structural acceleration $\boldsymbol{u}''$ of the substrate is imposed as normal acceleration on the fluid domain and an external load $\boldsymbol{F}_s$ due to the first order pressure on the substrate. The calculation of the acoustic pressure based on the Helmholtz equation (6) reduces the numerical effort, since viscous and thermal boundary layers do not have to be resolved. This approach was validated in a similar device against a full thermoviscous model in our previous work [5]. Furthermore, the micro channel boundaries made of PDMS are approximated by an impedance boundary condition using the acoustic impedance of PDMS Z_{PDMS}, while the attenuation of the SAW by the channel side walls is interpreted as an offset in the amplitude of the elastic surface deformation. Hence, the calculation of the acoustic fields in the PDMS domain is omitted, which further reduces the numerical effort. However, the electric potential is calculated in both the fluid and PDMS domain. At the interfaces between LN and PDMS or fluid, internal continuity is assumed in the calculation using the "Electrostatics" interface. The calculation is performed in frequency space assuming a harmonic time dependence with the excitation frequency f and the boundary conditions given in Fig. S2.

Once the surface displacement and the electric potential of the standing surface acoustic wave (sSAW) at the surface of the LN substrate were calculated, this field was used as boundary condition in reduced models. In this way, the numerical effort is greatly reduced, as the calculation of the acoustic and electric field quantities is limited to the fluid domain or fluid and PDMS domain, respectively. In turn, this enables a finer mesh resolution and parameter studies at the given resources. The reduced model for calculating the acoustic fields and acoustically induced fluid flow is described in detail in our previous study [5]. In Fig. S3, the reduced model for calculating the electric field quantities is depicted.

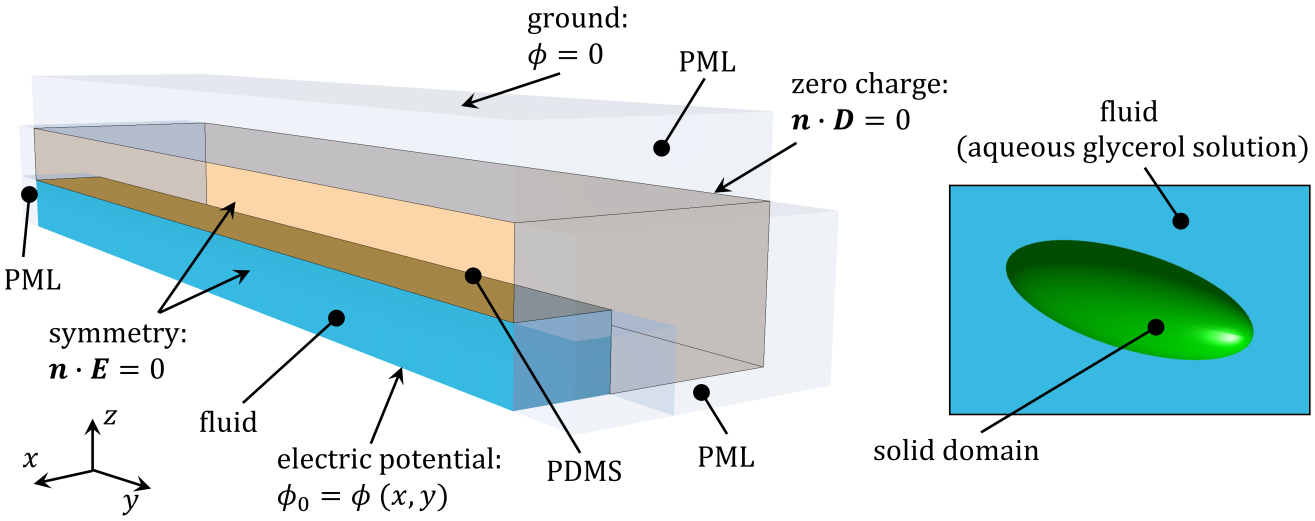

FIG. S3. Schematic representation of the reduced numerical model for calculating the electrical potential in the fluid and PDMS domain. To integrate the dielectrophoretic force and torque over the particle equilibrium surface, a prolate spheroid was added as a solid domain within the fluid domain.

Here, both the fluid and PDMS domains are incorporated and surrounded by PMLs. To calculate the dielectrophoretic force and torque on a prolate spheroid made of polystyrene, the particle is represented as a solid domain within the fluid. A symmetry boundary condition is set in the yz-plane at $x = 0\,\mu\text{m}$, analogous to the full numerical model. The calculation is performed in frequency space using the "Electrostatics" interface in Comsol Multiphysics (version 6.1, [4]). All material parameters used for the fluid, LN, polystyrene and PDMS are listed in Tab. S1. The numerical calculations were performed as parallel batch jobs on a high-performance computing cluster with AMD EPYC 7601 (2.2 GHz) processors and up to 2 TB of random-access memory (RAM).

B. Mesh independence

The convergence of the numerical solutions obtained from the full numerical model was analyzed with mesh refinement in a reduced domain featuring only 10 electrode pairs. Second-order tetrahedral mesh elements were used to discretize the computational domain. The mesh was refined towards the substrate surface, while a maximum element size of $\lambda_{\text{SAW}}/10$ was set in the fluid domain. Using the relative convergence function C, the numerical solutions g were compared for an increasing mesh refinement according to [13]

$$C(g) = \sqrt{\frac{\int_A (g - g_{\text{ref}})^2 \, dA}{\int_A g_{\text{ref}}^2 \, dA}}. \tag{S1}$$

Here, g_{ref} and A denote the reference solution obtained with the highest mesh resolution and the area of the fluid-LN interface, respectively. By increasing the number N of mesh elements per wavelength of the SAW on the substrate surface, convergent curves for the amplitude of the sSAW A and the time-averaged absolute electric potential $\langle|\phi|\rangle$ are evident in Fig. S4a. Taking into account the increasing amount of degrees of freedom (DOF) of the numerical model and the associated increasing need for RAM, a relative convergence of $C \leq 5 \times 10^{-3}$ is assumed to be sufficient. This threshold is achieved for both A and $\langle|\phi|\rangle$ with $N = 13$. In all further numerical investigations, the maximum element size is kept constant at $\lambda_{\text{SAW}}/13$ at the substrate-fluid interface.

The calculated normal surface displacement and electric potential at the substrate surface are used as boundary conditions in the reduced models. For a mesh independence study of the reduced model to calculate the acoustic field quantities, the interested reader is referred to Sachs et al. (2023) [5]. The relative convergence of the time-averaged absolute electric potential and electric field in the fluid domain are shown in Fig. S4b as a function of the number of mesh elements per wavelength of the bulk acoustic wave (BAW) N. Here, the integration according to Eqn. S1 was performed across the volume V of the fluid domain. In the corresponding simulations, a non-spherical particle was not considered. Since the electric field was calculated as a gradient of the electric potential according to Eqn. 5, a slower convergence is evident. However, C drops below the threshold of $C = 5 \times 10^{-3}$ at $N = 12$ for both field quantities. The corresponding mesh was used in all further numerical simulations.

When a prolate spheroid is incorporated into the fluid domain, the mesh was highly refined towards the particle surface. A mesh independence study on the maximum element size D_{p} on the particle surface in Sachs et al. (2023) [5] resulted in a sufficiently fine mesh for $D_{\text{p}} \approx 0.106\,\mu\text{m}$. This corresponds to $\delta_{\text{v}}/D_{\text{p}} = 1.45$ and was adopted for the

TABLE S1. Material properties at $T_0 = 25$ °C used in the numerical calculations.

Quantity	Symbol	Value
Fluid (water - glycerol mixture 76/24 v/v)		
Density[6]	ρ_0	1.0666 g/cm^3
Speed of sound[7]	c_0	1619.6 m/s
Shear viscosity[6]	μ_0	2.026 mPa s
Bulk viscosity[8][a]	μ_b	2.485 mPa s
Thermal conductivity[6]	k_th	0.4962 W/(m K)
Heat capacity at const. pressure[6]	$C_{\mathrm{p},0}$	3695 J/(kg K)
Heat capacity ratio[9][b]	γ	1.011
Relative permittivity[c]	$\epsilon_{\mathrm{r},0}$	69.03
Electric conductivity	σ_c	$6\,\mu\mathrm{S\,m^{-1}}$
128° YX Lithium niobate ($LiNbO_3$)		
Density[d]	ρ_s	4.64 g/cm^3
Elasticity tensor[10][e]	$\boldsymbol{c}$	$\begin{bmatrix} 2.030 & 0.701 & 0.579 & 0.1285 & 0 & 0 \\ 0.701 & 1.944 & 0.908 & 0.097 & 0 & 0 \\ 0.579 & 0.908 & 2.221 & 0.085 & 0 & 0 \\ 0.129 & 0.097 & 0.085 & 0.758 & 0 & 0 \\ 0 & 0 & 0 & 0 & 0.570 & -0.051 \\ 0 & 0 & 0 & 0 & -0.051 & 0.781 \end{bmatrix} \times 10^{11}\,\mathrm{N/m^2}$
Piezoelectric tensor[10][e]	$\boldsymbol{e}$	$\begin{bmatrix} 0 & 0 & 0 & 0 & 4.455 & 0.308 \\ -1.847 & 4.432 & -1.539 & 0.078 & 0 & 0 \\ 1.697 & -2.680 & 2.323 & 0.616 & 0 & 0 \end{bmatrix} \mathrm{C/m^2}$
Relative permittivity tensor[10][e]	$\boldsymbol{\epsilon}_\mathrm{r}$	$\begin{bmatrix} 44 & 0 & 0 \\ 0 & 38.314 & -7.277 \\ 0 & -7.277 & 34.686 \end{bmatrix}$
Polystyrene particles		
Density[f]	ρ_p	1.05 g/cm^3
Speed of sound[11]		
pressure waves	$c_{\mathrm{PS,p}}$	2350 m/s
shear waves	$c_{\mathrm{PS,s}}$	1120 m/s
Relative permittivity[12]	ϵ_PS	2.55
Polydimethylsiloxane		
Relative permittivity	ϵ_PDMS	2.75
Acoustic impedance	Z_PDMS	$1.04 \times 10^6\,\mathrm{Pa\,s\,m^{-1}}$

[a] Value taken for water.
[b] Value taken for water.
[c] Derived as $\epsilon_\mathrm{r} = w_\mathrm{g}\epsilon_\mathrm{g} + (1 - w_\mathrm{g})\epsilon_\mathrm{w}$ using the relative permittivity of glycerol ϵ_g [11] and water ϵ_w [11] as well as the mass fraction of glycerol w_g.
[d] As provided by the manufacturer (Siegert Wafer GmbH).
[e] A tensor rotation about the Euler angles (0°,38°,0°) was applied.
[f] As provided by the manufacturer (MicroParticles GmbH).

integration of both the acoustic and dielectrophoretic force and torque. Here, $\delta_\mathrm{v} = \sqrt{\mu_0/(\pi f \rho_0)}$ represents the viscous boundary layer thickness.

III. PARTICLE AGGLOMERATION AT THE EDGE OF THE THIN METAL LAYER

The transition from the free to the metallized substrate surface represents a discontinuity in the electrical boundary conditions, resulting in gradients in the electric field at the edge of the metal layer. As a consequence, the dielectrophoretic (DEP) force potential ξ on spherical particles changes in y-direction, as shown in Fig. S5 in the yz-plane at $x/\lambda_\mathrm{SAW} = -0.27$ using numerical calculations. In the corresponding numerical model, a "Dielectric Shielding" boundary condition [4] was set for $y/AP > 0$ at the interface between fluid and LN substrate. The DEP force on suspended particles is directed antiparallel to gradients in ξ, indicating a local force acting from the free to the metallized substrate surface.

When the particles first pass the metal layer and then the free substrate surface in the experiment, the DEP force thus acts antiparallel to the main flow direction. Furthermore, the main flow velocity and the Stokes drag force on suspended particles decrease towards the channel bottom due to no-slip boundary conditions. If the DEP force locally exceeds the Stokes drag force, particles get trapped in the vicinity of the edge of the metal layer. This phenomenon is depicted in Fig. S6 by images of spherical particles at different time instants after switching on the sSAW. In the experiments, a cylindrical lens in front of the camera caused optical distortions of the particle images, which were used

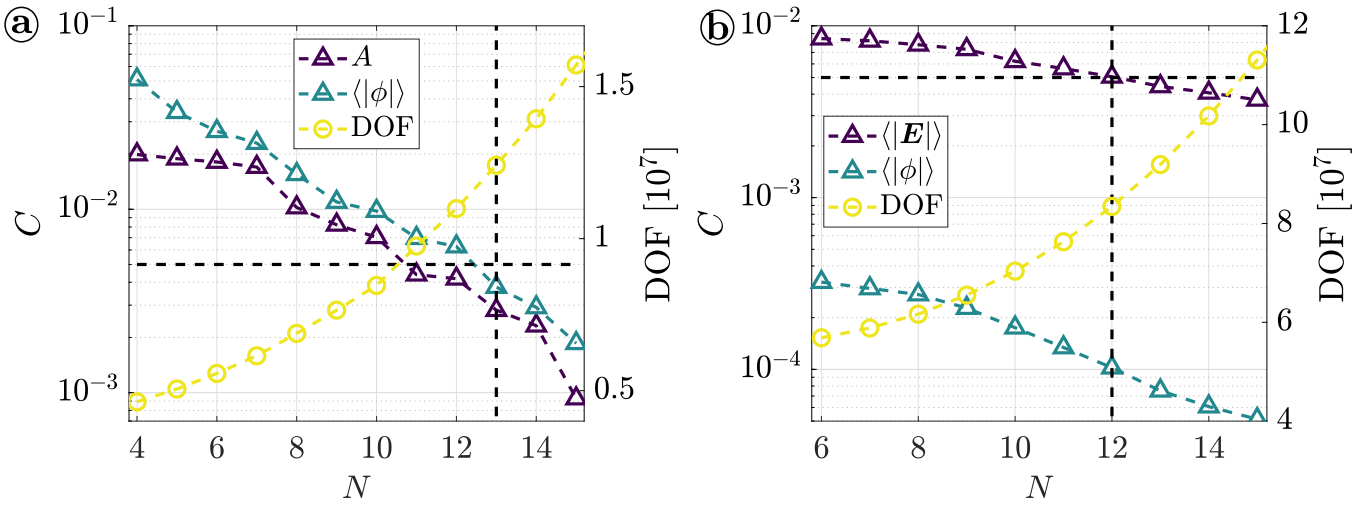

FIG. S4. (a) Relative convergence C as a function of the number of mesh elements per wavelength N for the amplitude of the sSAW A and the time-averaged absolute electric potential $\langle|\phi|\rangle$ at the substrate surface below the fluid domain, calculated in the full model. The degrees of freedom in the numerical calculation are indicated by DOF. The reference solution is calculated with $N = 16$. The threshold of $C = 5 \times 10^{-3}$ is reached at $N = 13$ as indicated by black dashed lines. (b) Relative convergence of the time-averaged magnitude of the electric field $\langle|\boldsymbol{E}|\rangle$ and the time-averaged absolute electric potential $\langle|\phi|\rangle$ in the fluid domain as calculated based on the reduced numerical model.

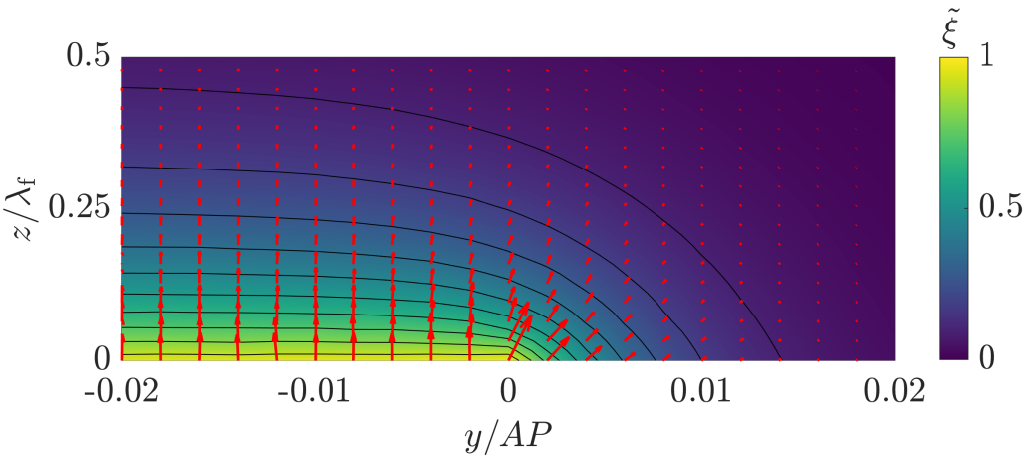

FIG. S5. Numerically calculated normalized dielectrophoretic force potential $\tilde{\xi}$ at the edge of the metal layer ($y/AP = 0$) and in vicinity to the channel floor. The magnitude and direction of the dielectrophoretic force in the yz-plane is indicated by red arrows.

in astigmatism particle tracking velocimetry (APTV) measurements to determine the depth position of the spherical particles [14]. The particles are forced to stable x-locations near the pressure nodes of the sSAW with a distance of $\lambda_{SAW}/2$. In the metallized region, the particles close to the channel floor are following the pressure-driven main flow in negative y-direction until they agglomerate at the edge of the metal layer over time. However, as the effect of the DEP force is limited to the immediate vicinity of the substrate surface, particles can pass the edge of the metal layer at higher levels. Once the sSAW was deactivated, the particles were carried away with the main flow. This effect could be used in tailored acoustofluidic devices with multiple metal layers for sequential concentration of particles.

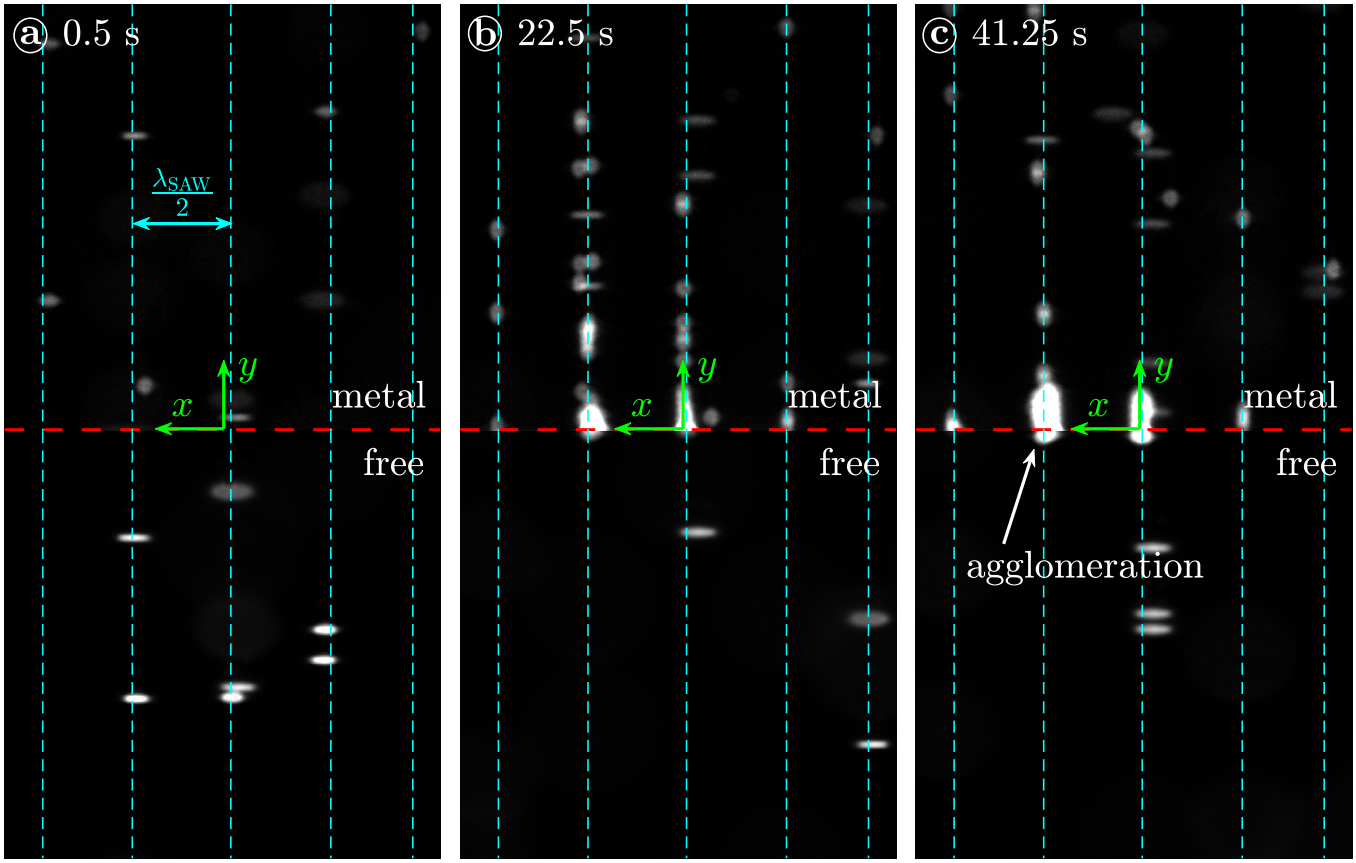

FIG. S6. Agglomeration of spherical particles at the edge of the thin metal layer (highlighted by the red dashed line) 0.5 s (a), 22.5 s (b) and 41.25 s (c) after activating the sSAW. Stable particle locations near pressure nodes of the sSAW are marked by dashed lines in cyan. A main flow at constant volume flow rate was applied from top to bottom (negative y-direction). Particle images appear elliptically distorted due to a cylindrical lens placed in the optical path to conduct APTV measurements.

IV. NUMERICALLY CALCULATED AMPLITUDE AND ELECTRIC POTENTIAL OF THE SSAW

The numerically calculated normalized amplitude $\tilde{A}$ and time-averaged absolute electric potential $\langle|\tilde{\phi}|\rangle$ are depicted across the substrate-fluid interface in the left and right half of Fig. S7, respectively. Both field quantities possess periodic structures with several nodes and antinodes along the channel width. When comparing both fields, it shows that the positions of antinodes coincide between $\tilde{A}$ and $\langle|\tilde{\phi}|\rangle$.

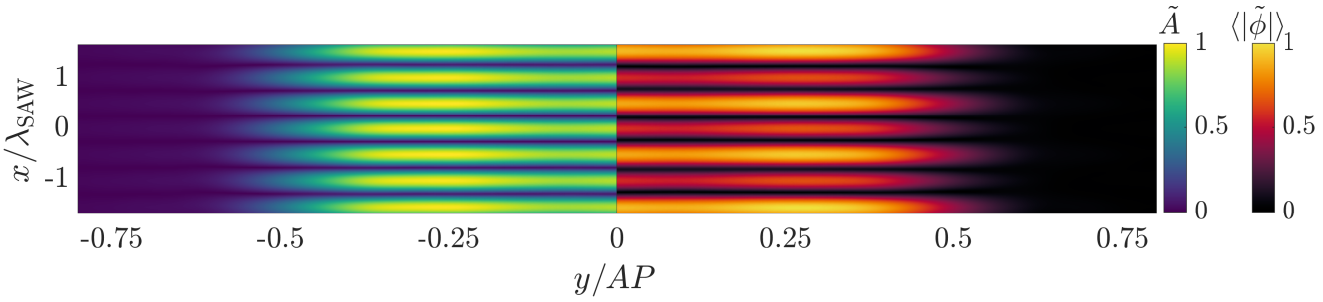

FIG. S7. Numerically calculated normalized amplitude (left half) and time-averaged absolute electric potential (right half) of the sSAW at the substrate surface underneath the fluid.

V. VORTEX FORMATION IN THE OUTER REGION OF THE SSAW

In the outer regions of the aperture AP sharp gradients in the amplitude of the SAWs are present (see Fig. 3). The resulting gradients in the acoustic pressure field drive complex three-dimensional acoustically induced vortex structures as shown in Fig. S8 calculated with numerical simulation. While the acoustically induced fluid flow in the center of the sSAW exhibits velocity components only in the xz-plane, significant velocity components occur in all spatial directions in the outer regions. The calculated velocity field agrees qualitatively with experimental investigations at various wavelengths of the sSAW λ_{SAW} and channel heights [2]. The position and orientation of the suspended particles are significantly influenced by the existing vortex patterns when entering or leaving the acoustoelectric wave field. However, the velocity of the acoustically induced fluid flow can be reduced by increasing the wavelength λ_{SAW} or decreasing the channel height [2].

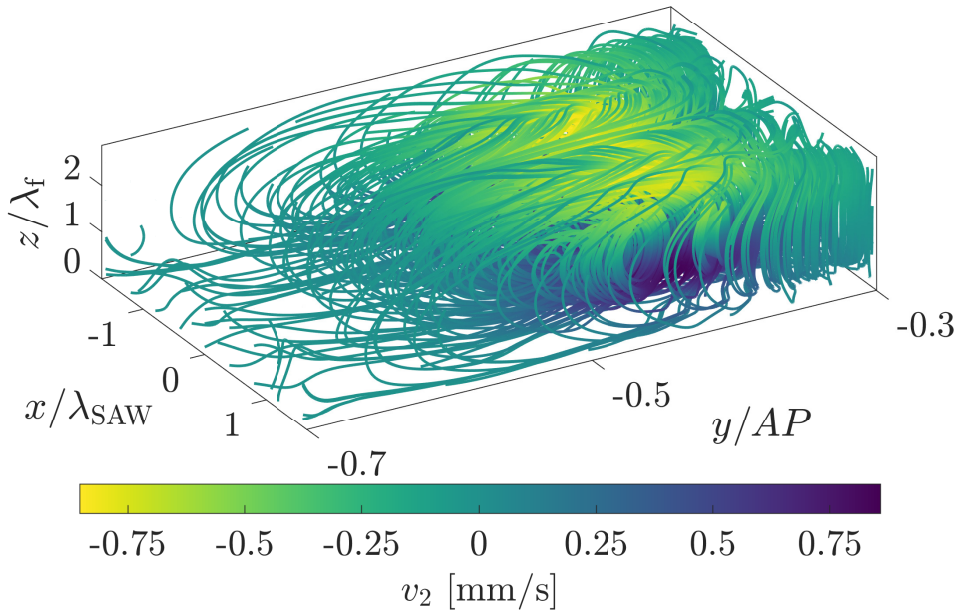

FIG. S8. Three-dimensional acoustically induced fluid flow in the outer region of the fluid domain indicated by streamlines as a result of a numerical simulation. The streamlines are color-coded by the velocity component v_2 in y-direction.

VI. OUT-OF-PLANE ORIENTATION OF PROLATE SPHEROIDS IN THE ACOUSTOELECTRIC WAVE FIELD

The images of suspended prolate spheroids allow the determination of the in-plane orientation of the particles in the xy-plane. To analyze the out-of-plane orientation of the particles, e.g. by using the lengths of the major and minor axes of the particle image, the particle has to be aligned perpendicular to the observation direction and focused in the xy-plane at least once during the observation [5]. This requirement cannot be ensured in the experiments carried out with the particles suspended in an pressure-driven main flow. However, the intensity of the particle image depends on the distance of the particle to the focal plane. If a prolate spheroid possesses an out-of-plane orientation $\theta \neq 90°$, the position of the maximum intensity shifts away from the center of the corresponding particle image. This phenomenon was observed experimentally, as shown in Fig. S9 using exemplary images of particles in the acoustoelectric wave field. The maximum intensity of the exemplary particle images is eccentrically located either to the right or left of the center of the particle image. Since all particle images were taken with the same focus position and the particles were focused on stable positions in the acoustoelectric wave field, it is reasonable to assume that the particles were at a similar z-position. Hence, it is likely that the particles were oriented with either an out-of-plane angle $\theta \approx \theta'$ or $\theta \approx \theta''$. Both orientations are found to be stable based on the numerical simulations (see Fig. 16).

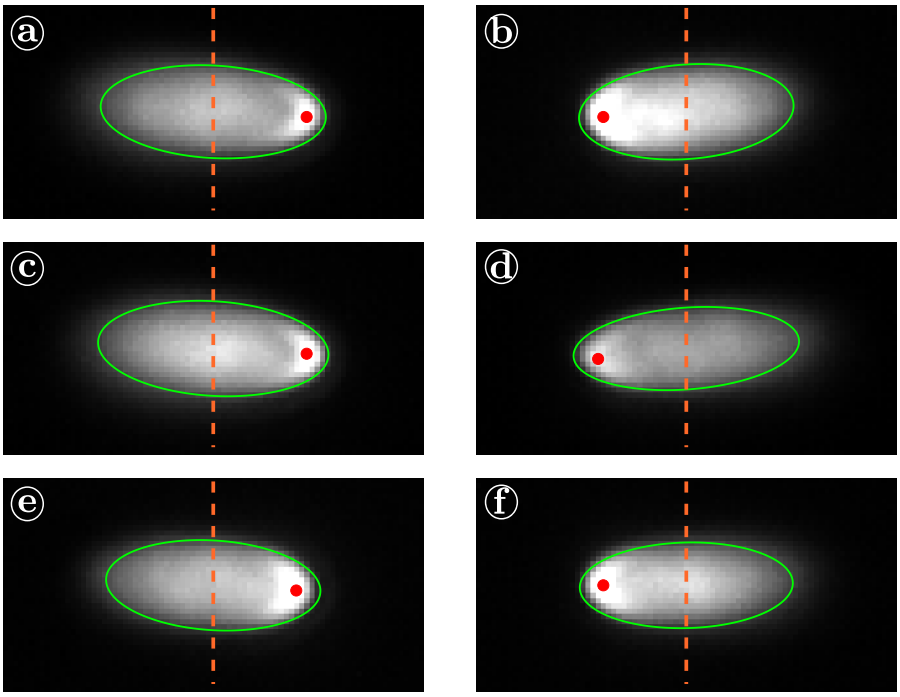

FIG. S9. Prolate spheroids detected above the free substrate surface at an in-plane orientation of $\varphi \approx 180°$. The central positions of the particles are highlighted by dashed lines in orange, while the highest intensity values were found eccentrically (on the right in (a, c, e) and on the left in (b, d, f)) as marked by red dots.

[1] A. Fakhfouri, C. Devendran, T. Albrecht, D. J. Collins, A. Winkler, H. Schmidt, and A. Neild, Surface acoustic wave diffraction driven mechanisms in microfluidic systems, Lab on a Chip **18**, 2214 (2018).
[2] S. Sachs, C. Cierpka, and J. König, On the acoustically induced fluid flow in particle separation systems employing standing surface acoustic waves - Part II, Lab on a Chip **22**, 2028 (2022).
[3] M. W. H. Ley and H. Bruus, Three-dimensional numerical modeling of acoustic trapping in glass capillaries, Physical Review Applied **8**, 2 (2017).
[4] Comsol multiphysics, version 6.1 (2024).
[5] S. Sachs, H. Schmidt, C. Cierpka, and J. König, On the behavior of prolate spheroids in a standing surface acoustic wave field, Microfluidics and Nanofluidics **27**, 81 (2023).
[6] I. H. Bell, J. Wronski, S. Quoilin, and V. Lemort, Pure and pseudo-pure fluid thermophysical property evaluation and the open-source thermophysical property library coolprop, Industrial & Engineering Chemistry research **53**, 2498 (2014).
[7] L. Negadi, B. Feddal-Benabed, I. Bahadur, J. Saab, M. Zaoui-Djelloul-Daouadji, D. Ramjugernath, and A. Negadi, Effect of temperature on density, sound velocity, and their derived properties for the binary systems glycerol with water or alcohols, The Journal of Chemical Thermodynamics **109**, 124 (2017).
[8] M. J. Holmes, N. G. Partiker, and Povey M J W, Temperature dependence of bulk viscosity in water using acoustic spectroscopy, J. Phys. Conf. Ser. **269**, 012011 (2011).
[9] R. Barnkob, N. Nama, L. Ren, T. J. Huang, F. Costanzo, and C. J. Kähler, Acoustically driven fluid and particle motion in confined and leaky systems, Physical Review Applied **9**, 014027 (2018).
[10] B. A. Auld, *Acoustic fields and waves in solids - volume 1* (Robert E. Krieger publishing company inc, 1973).
[11] W.M. Haynes, *Handbook of Chemistry and Physics* (CRC Press, Boca Raton, 2014).
[12] M. Tayebi, D. Yang, D. J. Collins, and Y. Ai, Deterministic sorting of submicrometer particles and extracellular vesicles using a combined electric and acoustic field, Nano letters **21**, 6835 (2021).
[13] P. B. Muller, R. Barnkob, M. J. H. Jensen, and H. Bruus, A numerical study of microparticle acoustophoresis driven by acoustic radiation forces and streaming-induced drag forces, Lab on a Chip **12**, 4617 (2012).
[14] C. Cierpka, R. Segura, R. Hain, and C. J. Kähler, A simple single camera 3C3D velocity measurement technique without errors due to depth of correlation and spatial averaging for microfluidics, Measurement Science and Technology **21**, 045401 (2010).